

See discussions, stats, and author profiles for this publication at: <https://www.researchgate.net/publication/239938818>

Nb-Doped TiO₂ Nanofibers for Lithium Ion Batteries

ARTICLE in THE JOURNAL OF PHYSICAL CHEMISTRY C · JULY 2013

Impact Factor: 4.77 · DOI: 10.1021/jp402498p

CITATIONS

27

READS

103

11 AUTHORS, INCLUDING:



Marcus Fehse

Chiang Mai University

8 PUBLICATIONS 69 CITATIONS

SEE PROFILE



Sara Cavaliere

Université de Montpellier

46 PUBLICATIONS 1,544 CITATIONS

SEE PROFILE



Iuliia Savych

Université de Montpellier

6 PUBLICATIONS 245 CITATIONS

SEE PROFILE



Lorenzo Stievano

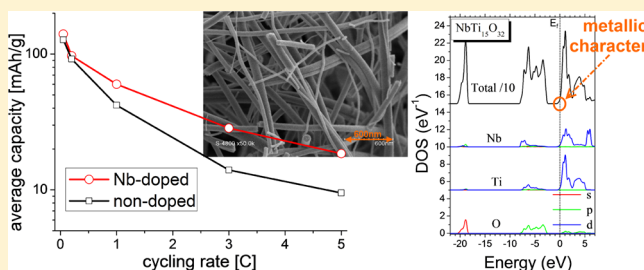
Université de Montpellier, Montpellier, France

132 PUBLICATIONS 1,662 CITATIONS

SEE PROFILE

Nb-Doped TiO₂ Nanofibers for Lithium Ion BatteriesM. Fehse,^{*,†} S. Cavaliere,[†] P. E. Lippens,[†] I. Savych,[†] A. Iadecola,[§] L. Monconduit,[†] D. J. Jones,[†] J. Rozière,[†] F. Fischer,[‡] C. Tessier,[‡] and L. Stievano^{*,†}[†]ICG-AIME UMR CNRS 5253 Université Montpellier 2, Place E. Bataillon, 34095 Montpellier Cedex 5, France[‡]SAFT, Direction de la Recherche, 111-113 Bd Alfred Daney, 33074 Bordeaux, France[§]Elettra-Sincrotrone Trieste, Strada Statale 14, 34149 Basovizza, Italy

ABSTRACT: Niobium-doped nanofibers elaborated by facile, single-step electrospinning present a higher rate capability in electrochemical cycling experiments than nondoped materials. This is attributed to the reduction of Li⁺ diffusion path lengths and enhanced intimate interparticle contact, in combination with improved intraparticle conductivity. Niobium doping has a significant effect on the electronic structure and provokes a substantial decrease in particle size.



1. INTRODUCTION

Since their introduction into the market in the early 1990s by Sony, lithium ion batteries (LIBs) have come a long way.¹ Originally intended to serve only for small portable electronic devices, they have conquered numerous other fields of domestic and military applications and have become an indispensable component of present day technologised society. Today LIBs are at the dawn of entering not only the transportation market on the large scale, but also to backbone the transition from fossil to renewable energy sources. In this development, graphite, which is today's commercially established anode material, has limited high cycling rate properties due to necessary solid electrolyte interphase (SEI) formation and the risk of lithium plating when overcharged due to its low working potential. An elevated performance is however crucial for application in the transportation sector, not only for rapid acceleration but also for reduced recharging times and recovery of braking energy. In the search of alternative anode materials, TiO₂ has been widely recognized as a viable candidate due to its cost effectiveness, environmental benignancy, and lithium storage capability. Of particular interest is its tetragonal polymorph, the anatase phase. It has a high theoretical capacity (335 mAh/g), a flat operating potential, and low volume expansion (ca. 3%) during Li⁺ charge/discharge leading to long cycle life and durability.²

However, the poor electronic conductivity (ca. 10⁻¹²–10⁻⁷ S/cm), the frequent aggregation of titania nanoparticles, and the low Li⁺ diffusion rate (ca. 10⁻¹⁵–10⁻⁹ cm²/s) reduce the electrochemical performance of anatase-TiO₂. Considerable efforts have been made to overcome the ionic and electronic transport limitation of titania anodes.^{3–6} One approach is the tailoring of the morphology and particle size of TiO₂-based materials. In this respect, one-dimensional (1D) nanostructured materials such as nanofibers and nanotubes are particularly interesting for LIBs, due to their large surface/volume ratio,

their vectorial electron (along the long dimension) and Li⁺ (along the lateral direction) transport properties, and their ability to accommodate lithiation-induced stresses.^{7,8}

Soft-chemistry and template-based syntheses are usually employed to synthesize fibrous nanostructured electrodes.^{9–12} Among the methods for generating 1D nanostructures, electrospinning is a simple and versatile technique for preparing ultrathin nanofibers and nanotubes of polymers,¹³ composites,¹⁴ and ceramics¹⁵ with controlled and reproducible diameters. Recent years have witnessed a growing development of electrospun TiO₂-based electrodes for lithium-ion batteries, fuel cells, and other conversion and energy storage devices.^{16–20}

Various methods are pursued to further enhance the performance of electrospun titania when used as an active insertion material in LIBs. One of them is the preparation of composite nanostructured electrodes interconnecting titania with a conducting additive nanophase (based on carbon), which improves the electron transfer. With this aim, porous carbon nanofibers loaded with TiO₂ nanoparticles,²¹ composite TiO₂/C,²² and TiO₂/graphene nanofibers²³ with improved reversible capacity and high rate behavior have been recently reported. Another approach is surface modification to promote faster Li⁺ diffusion and electron transport but also to suppress particle agglomeration.²⁴ For instance, the layer-by-layer self-assembly approach was combined with electrospinning for the fabrication of MoO₃-modified TiO₂ nanohybrids with improved lithium-storage properties, compared to the uncoated materials.²⁵ A further approach to enhance the electrical conductivity of TiO₂ nanofibers is loading them with metal nanoparticles. LIB anodes based on electrospun titania nanofibers embedding 10% Au or Ag nanoparticles showed a 20% enhancement of the

Received: March 12, 2013

Revised: May 22, 2013

Published: June 5, 2013

specific capacity and a 2-fold rate performance compared to the bare TiO_2 .²⁶ TiO_2/Ag composite nanotubes fabricated by coaxial electrospinning also showed increased rate performance and cycling stability.²⁶

Doping with aliovalent ions is also a facile strategy to modify the electronic properties of electrospun titanium oxide.^{17,18,27–30} Nevertheless, only few papers report this procedure for application of the materials in LIBs.³¹ This is astonishing as, for example, Wang et al. show that the conductivity, which is the crucial parameter for high performance cycling, can be raised 2 orders of magnitude by doping mesoporous TiO_2 with Nb.³² These findings are in agreement with the results of Archana et al. stating an enhanced Li^+ mobility and diffusion coefficient for Nb-doped TiO_2 electrospun fibers³³ as well as findings by Sheppard et al. describing metallic-type conduction behavior of Nb-doped TiO_2 .³⁴

In the present paper, we report the synergistic effects of nanostructuring by electrospinning and doping with niobium on TiO_2 anode materials for lithium-storage applications. Nanofibrous TiO_2 with and without Nb doping is synthesized via electrospinning and characterized via XRD, SEM, and XAS. Furthermore, we provide results from DFT calculations to explain in detail the effect of Nb doping on electronic band structure, explaining the observed increase of the electronic conductivity. The potency of the nanofibers as a lithium insertion material was tested by preparing film electrodes and applying them in half-cells vs lithium. Simple, standardized synthesis and electrode preparation methods were chosen to elucidate only the effect of Nb doping on the electrochemical cycling properties, avoiding possible pseudocapacitive storage contribution from morphology tailoring or enhanced conductivity by elaborated electrode formulation, as these might superimpose to the effects of the dopant and hence disguise its benefits.

2. EXPERIMENTAL SECTION

2.1. Synthesis of 10% Nb-Doped and Nondoped TiO_2 Nanofibers. The detailed synthesis of titania nanofibers has already been reported elsewhere.¹⁷ Briefly, the carrier polymer solution based on polyvinyl pyrrolidone (average $M_w \approx 1\,300\,000$ g/mol, Aldrich) in absolute ethanol (puriss., Sigma-Aldrich) was mixed with a solution containing 0.52 mL of titanium(IV) isopropoxide (97%, Aldrich), 0.040 mL of niobium ethoxide (99.95%, Aldrich), and 1 mL of acetic acid (Sigma-Aldrich), corresponding to a dopant content of 10 at. %. Electrospinning of the final solution was carried out in air at room temperature with a standard syringe and a grounded collector plate configuration. The distance between the needle tip and the collector plate was 10 cm, the applied voltage 15 kV, and the flow rate 0.5 mL/h. The as-prepared fibers were calcined in air at 500 °C at a heating rate of 5 °C/min for 6 h in order to remove the carrier polymer.

2.2. Electrode and Cell Preparation. For electrochemical measurements, the titania powder which serves as an active insertion material was mixed with carbon black and PVdF with a weight composition of 80:8:12, respectively. An NMP-based slurry of this mixture was tape casted on a copper foil using a doctor blade system leading to homogeneous $\sim 25\ \mu\text{m}$ thick films which were cut and used as the working electrodes. These were built in Swagelok cells together with lithium metal as reference and counter electrode as well as Whatman fiber glass separators. A standard mixture of organic solvents containing ethylene carbonate, propylene carbonate, and dimethyl

carbonate in composition 1:1:3 and 1 M LiPF_6 was used as the electrolyte. Since both electrolyte and lithium metal are very sensitive to air and moisture, the assembly of the electrochemical cells was carried out in a glovebox under Ar atmosphere.

2.3. Characterization. The nanofiber morphology was verified by using a scanning electron microscope (SEM) Hitachi S-4800 FEG equipped with energy-dispersive spectroscopy analysis (EDS) and a JEOL 1200 EXII transmission electron microscope (TEM) operating at 120 kV equipped with a CCD camera SIS Olympus Quemesa (11 million pixels). The crystal structures were identified by powder X-ray diffraction (XRD) using a Philips X'pert diffractometer with $\text{Cu K}\alpha$ radiation at room temperature, in the range from 10 to 70° 2 θ using a step size of 0.026° and dwell time of 3500 s. Fullprof was used for determination of unit cell parameters (Rietveld refinement). Nitrogen physisorption was carried out on a Micromeritics ASAP2020, and the adsorption and desorption isotherms were analyzed using the Brunauer–Emmett–Teller (BET) as well as density functional theory (DFT) methods to calculate specific surface area and pore size distribution, respectively.

The surface composition of the nondoped and Nb-doped TiO_2 fibers was monitored by X-ray photoelectron spectroscopy (XPS) on an ESCALAB 250 (Thermo Electron). The X-ray excitation was provided by a monochromatic Al $\text{K}\alpha$ (1486.6 eV) source with a beam diameter of 400 μm . A constant analyzer energy mode was used for the electron detection (20 eV pass energy). The detection of the emitted photoelectrons was performed perpendicularly to the sample surface. Data quantification was performed with the Advantage program. The background signal was removed using the Shirley method. The surface atomic concentrations were determined from photoelectron peaks areas using the atomic sensitivity factors reported by Scofield. Binding energies (BEs) of all core levels were referred to the C–C bond of C 1s at 284.8 eV.

Raman spectroscopy was carried using LabRam ARAMIS IR², Horiba Jobin Yvon with a blue diode laser $\lambda = 473$ nm or helium neon laser $\lambda = 633$ nm.

XAS measurements were carried out at ambient temperature on the beamlines A (HASYLAB @ DESY, Hamburg, Germany) and XAFS (ELETTRA, Trieste, Italy). The Ti K-edge spectra were recorded in transmission mode on homogeneous pressed pellets of adequate thickness. Fourier transforms were performed using k^2 weighting, and the structural parameters were determined by curve-fitting procedures using Artemis data analysis software with embedded FEFF tool for calculating scattering paths on the basis of the anatase structure. To fit Nb-doped anatase in the R-space, FEFF paths based on Nb_2O_5 crystal structure in which the central Nb atom was exchanged for Ti were added, in order to include Ti–Nb bonds in the calculations.

Electronic structure calculations based on DFT and a generalized gradient approximation (GGA) using an exchange-correlation potential by Perdew, Burke, and Ernzerhof³⁵ were performed for anatase TiO_2 and three supercells of 24 atoms ($\text{NbTi}_7\text{O}_{16}$), 48 atoms ($\text{NbTi}_{15}\text{O}_{32}$), and 108 atoms ($\text{NbTi}_{35}\text{O}_{72}$) which correspond to Nb doping of about 12, 6, and 3%, respectively. The augmented plane-wave method + local orbital (APW+lo) as implemented in the WIEN2k code³⁶ was used with the muffin-tin radii $R_{\text{mt}}(\text{Ti}) = 2.0$ a.u., $R_{\text{mt}}(\text{O}) = 1.4$ a.u., and $R_{\text{mt}}(\text{Nb}) = 2.0$ a.u., the semicore states: Ti 3s, Ti 3p, O 2s, Nb 4s, and Nb 4p, the plane-wave cutoff:

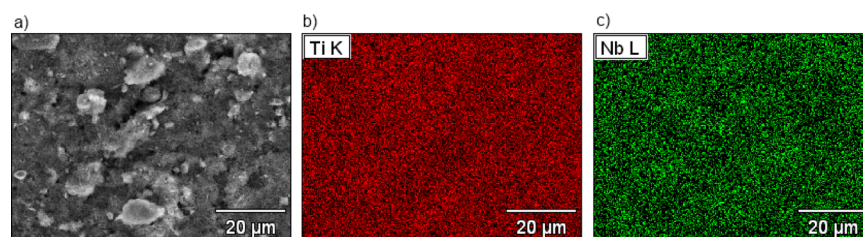


Figure 1. (a) EDX image and (b) elemental mapping of Ti and (c) Nb of tape casted film electrode.

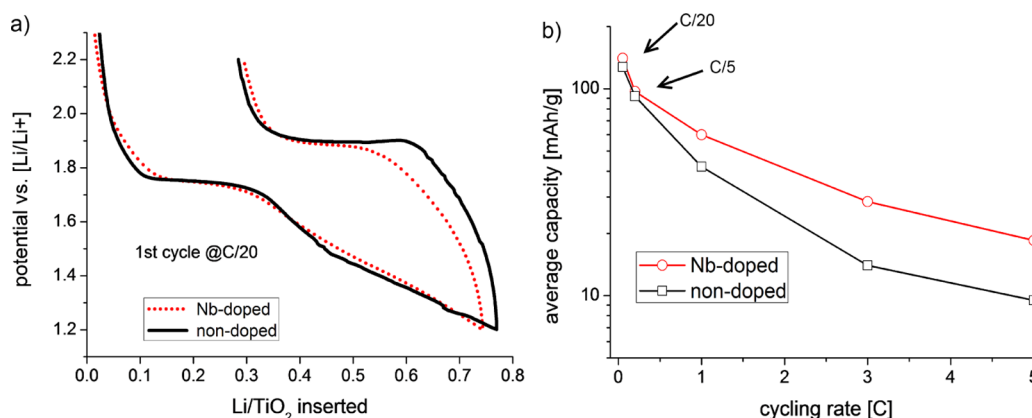


Figure 2. Comparison of (a) galvanostatic cycling curve and (b) mean rate capability of nondoped and Nb-doped electrospun TiO_2 nanofiber electrodes.

$\min(\text{Rmt}) \cdot \max(K) = 7$ (where K is a reciprocal lattice vector), and the magnitude of the largest vector in the charge-density Fourier expansion: $G_{\max} = 15 \text{ Ry}^{-1/2}$. The experimental values of the lattice constants were used for the calculations but the internal atomic positions were moved in order to minimize the internal atomic forces. A similar approach was successfully used for the electronic structure calculations of Sn^{37} and Zr^{38} -doped anatase TiO_2 . Self-consistency was achieved with an energy tolerance of 10^{-4} Ry and a force tolerance of $10^{-3} \text{ Ry bohr}^{-1}$. The XAS spectra were calculated from the dipole transition strengths and the partial density of states (PDOS) in the same way as previous calculations for $\text{Li}_4\text{Ti}_5\text{O}_{12}$.³⁹ The calculated Ti K-edge spectra were averaged over all the Ti atoms of the supercells. For comparison with experiments, the calculated spectra were convoluted with a Lorentzian function (fwhm = 2 eV).

The electrochemical cycling was carried out in galvanostatic mode on a Biologic multichannel potentiostat. Different cycling rates were applied ranging from C/20 to 5C, whereas 1C corresponds to the insertion of 1 Li per hour into TiO_2 which is equal to a current of 336 mA/g.

3. RESULTS

3.1. Electrode Properties and Electrochemical Characterization. Film electrodes were prepared via tape casting of slurries made of Nb-doped or nondoped $\text{TiO}_2/\text{C}/\text{PVdF}$ mixtures which resulted in homogeneous, uniform, and smooth film electrodes with a loading of Nb-doped or nondoped TiO_2 of roughly $1.5 \text{ mg}/\text{cm}^2$. Energy dispersive X-ray spectroscopy (EDS) analysis of such electrodes reveals a homogeneous distribution of active insertion material TiO_2 and dopant Nb; see Figure 1b and c, respectively. Furthermore, a Nb content of $8.1 \pm 0.2 \text{ at. \%}$ is determined from the ratio of Ti/Nb. This is close to the aspired value of 10 at. %, while at the same time no

unexpected elements were detected. EDS has a penetration depth of $\approx 10 \mu\text{m}$, assuring that the here stated value can be considered as the bulk concentration.

The galvanostatic cycling curves for the first cycle with doped and nondoped TiO_2 electrodes are presented in Figure 2a. The curves are quite similar, revealing typical insertion behavior of nanoscaled anatase with a plateau at 1.75 V which is followed by a slope which correspond to the biphasic and subsequent monophasic lithium insertion mechanism, respectively. It is noteworthy that the irreversible voltage plateau is less pronounced for the Nb-doped sample. In the first cycle, a high irreversibility is observed which suggests a SEI formation and trapping of Li^+ in irreversible sites. The samples were cycled 20 cycles at subsequently increased cycling rate, and the mean values of each cycling rate are presented in Figure 2b. Similar average capacity values at low cycling rates C/20 and C/5 are obtained for doped and nondoped TiO_2 , see Figure 2b, 140 vs 128 mAh/g and 97 vs 92 mAh/g, respectively. However, as the cycling rate is increased, a growing difference between the capacities obtained for doped and nondoped TiO_2 electrodes appears, while no general difference between the galvanostatic cycling curves is observed (not shown here). Although the overall capacity values are well below those found by Wang et al. (142 and 108 mAh/g @ C/4 and 1C, respectively, for mesoporous Nb-doped TiO_2 with a specific surface of $128 \text{ m}^2/\text{g}$),³² the direct comparison of nondoped and Nb-doped material reveals a superior high rate capability of the Nb-doped sample. At the highest cycling rate 5 C, the doped samples achieve double the capacity of nondoped TiO_2 , 23 vs 10 mAh/g. This phenomena of increased rate capability while maintaining absolute capacities was also recently reported for N-doped TiO_2 fibers.³¹

In order to elucidate the reason for this significant improvement in rate capability, a series of characterization

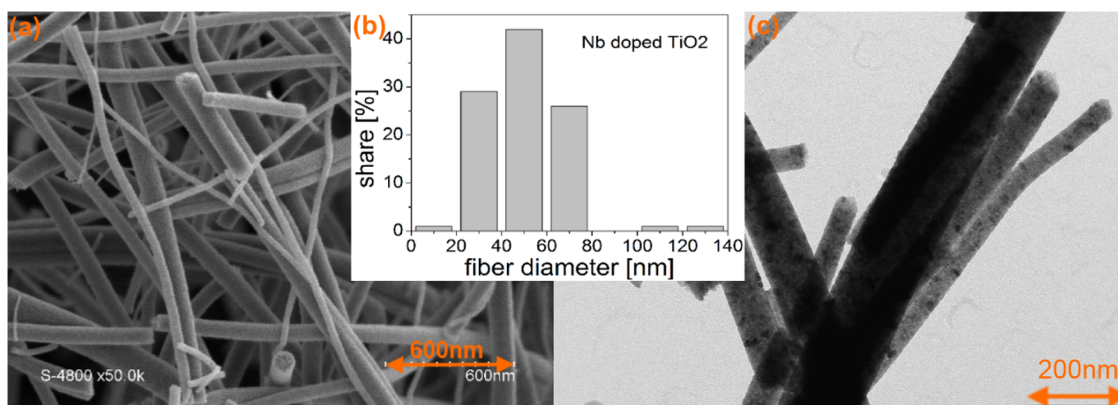


Figure 3. (a) SEM and (c) TEM micrographs of Nb-doped electrospun TiO_2 nanofibers and (b) distribution of fiber diameter.

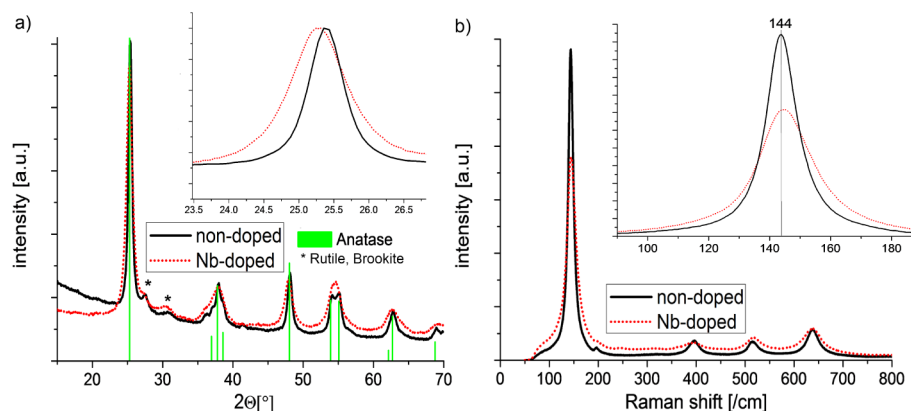


Figure 4. (a) XRD diffractogram with anatase reference (ICSD 009853) and (b) Raman spectra comparison of nondoped and Nb-doped TiO_2 nanofibers, showing the complete survey and an enlarged cutout of the most intense signal.

techniques and calculations were performed which illuminate the diverse influence of Nb doping on electrospun TiO_2 fibers.

3.2. Morphology. In Figure 3, the (a) SEM and (c) TEM micrographs show the morphology of the electrospun Nb-doped TiO_2 nanofibers. Uniform polycrystalline fibers with an average diameter of 51 ± 19 nm are obtained, whereas the length can reach several micrometers. Note that the TEM contrast variations reflect the polycrystalline microstructure of the fibers, consisting of well grown nanocrystals with different orientations. The graph in Figure 3b shows the diameter distribution, revealing the conformity of the nanofiber morphology, with $\geq 95\%$ of all values falling into the narrow range of 20–80 nm. SEM and TEM of nondoped TiO_2 show an equally narrow fiber distribution of diameter with a slightly higher average diameter of about 62 nm (not presented here). This small difference agrees with our previous observations¹⁷ and with the findings by Archana et al.³³ but is in opposition to the results of An and Ahn,⁴⁰ who showed rather a slight increase in the diameter of the fibers on Nb doping. It should be pointed out though that in any of these cases the magnitude of changes in diameter is small.

The results of nitrogen physisorption reveal also a great conformity of doped and nondoped samples. A type IV physisorption isotherm⁴¹ is observed which indicates mesoporosity, and a BET specific surface area of 66 and 44 m^2/g for doped and nondoped sample, respectively, was determined (not shown). We attribute this gain in specific surface area mainly to the reduced grain size, as pointed out in section 3.3. The similarity of the results is in agreement with the

assumption that Nb doping has no significant influence on the global morphology of TiO_2 electrospun nanofibers, as shown in previous work.¹⁷

3.3. Crystal Structure. When comparing the crystal and local structure of doped and nondoped samples by XRD and Raman spectroscopy (Figure 4), we find a clear signature of the anatase phase of both samples and no visible segregation of possible Nb-containing phases. While the Raman spectra in Figure 4b reveal a single anatase phase, the XRD patterns in Figure 4a show very minor traces of rutile as well as brookite in both samples, which is coherent with previous findings. The discrepancy between these two results is due to the lower sensitivity of Raman spectroscopy compared to XRD. In the XRD patterns, we find besides a peak broadening, corresponding to a crystallite size reduction from 15 to 7 nm determined using the Scherrer equation, a slight but significant peak shift to lower diffraction angles for the Nb-doped samples. According to Ruiz et al., Nb doping obstructs grain coarsening, which Guidi et al. attribute to the reduced ionic oxygen mobility.^{42,43} The XRD peak shift corresponds to an increase of lattice parameter a (3.789 Å, ICSD009853) of ~ 0.014 Å equivalent to ~ 3.7 . Whether this expansion is due to the larger ionic radius of Nb^{5+} (0.64 Å) compared to that of Ti^{4+} (0.61 Å), or a strengthening in Coulombic repulsion force between Nb and Ti cannot be answered at this point with certainty. Our findings are in agreement with the general idea of lattice expansion through substitutional doping of Ti by Nb, except that the magnitude of expansion is somewhat smaller than those found in the literature.^{40,42,44,45} This is likely to be related to the

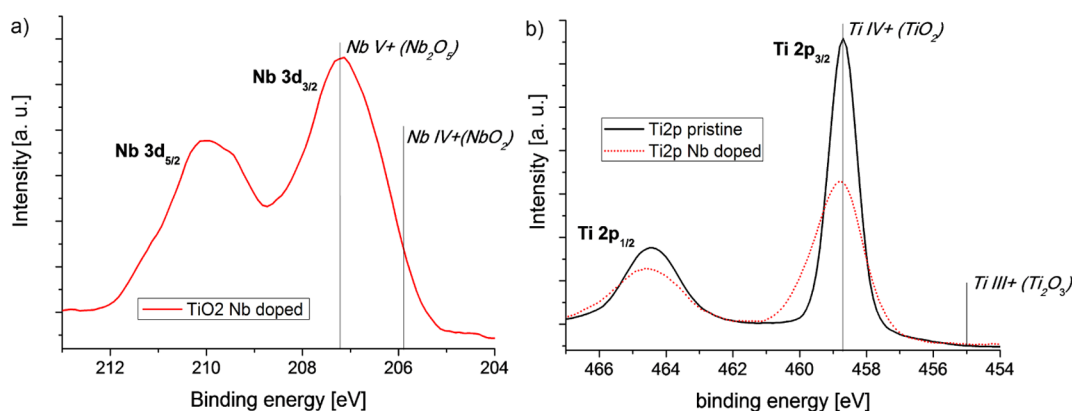


Figure 5. XPS spectra (a) Nb 3d peaks and (b) Ti 2p peaks comparison of doped and nondoped electrospun TiO_2 nanofibers.

influence of the nanostructuring on the lattice parameter which already accounts for an expansion of ~ 2.4 compared to the reference value.⁴⁶

3.4. Surface Composition Analysis. The Raman spectra show exclusively the typical bands of anatase, Figure 4b. A closer look reveals however small differences in the Nb-doped TiO_2 spectra. Not only a blue shift of the characteristic E_g band by $\sim 1 \text{ cm}^{-1}$ from the reference value of 144 cm^{-1} ⁴⁷ is observed, but also a deformation of the line shape. This asymmetry might result from the sum of a distribution of peaks reflecting a slight inhomogeneous Nb distribution. In addition, the creation of defects through doping is contributing to the observed peak broadening. The E_g band corresponds to the O–Ti–O bending vibration. If applying the harmonic oscillator model, the exchange of Ti for the heavier Nb atom should lead to a shift to lower wavenumber unless this change in mass is compensated by increased binding energy. Using the example of substitutional doping of Ti by Zr in TiO_2 , Lejon and Österlund attributed the observed Raman blue shift to surface stresses as well as spatial phonon confinement effects linked to Zr-doping-induced decrease of particle size, while at the same time an expansion of the lattice parameter is observed.⁴⁸ Ruiz et al. have described a direct relation between Raman line shift and expansion of lattice parameters, which substantiates the insertion of Nb dopant in the TiO_2 lattice;⁴² analogous results are published by Babu et al. for substitution of oxygen by N dopant in TiO_2 .²⁸

Since the structural characterization does not provide sufficient proof of Nb presence in the TiO_2 lattice, XPS measurements were carried out. XPS spectra of the nanofibers are presented in Figure 5a, showing characteristic Nb 3d twin peaks for the Nb-doped sample and in Figure 5b comparison of Ti 2p signals for nondoped and Nb-doped TiO_2 nanofibers. Ti $2p_{1/2}$ and Nb $3d_{3/2}$ peaks appear at 458.7 and 207.2 eV, respectively, indicating that titanium is present as Ti^{IV+} and niobium as Nb^{V+} . No signs of Ti^{III+} (455 eV⁴⁹) or Nb^{IV+} (205.9 eV⁵⁰) are visible in the spectra. These results foster the assumption that an effective aliovalent doping is accomplished. Furthermore, we can deduce that charge compensation of Nb^{V+} is not achieved by reducing Ti^{IV+} to Ti^{III+} but more likely by producing oxygen vacancies in the anatase lattice. It is nevertheless noteworthy that when interpreting XPS data of doped, high-specific-surface-area, nanostructured samples one has to take due care as surface state effects, change in Fermi level position, and band bending are influencing the peak position.^{5,42,51}

From quantification measurements, we obtained a Nb-to-Ti ratio of $\sim 16\%$ which denotes a slight agglomeration of Nb on the surface compared to the expected 10% bulk concentration. This suggests the segregation of Nb at the surface of electrospun TiO_2 fibers. According to the literature, it is mainly the oxygen activity and oxygen affinity of the dopant that determines whether or not surface segregation occurs.^{52,53} The possibility of inhomogeneous Nb dopant distribution is not considered, since the high solubility of Nb in TiO_2 is widely known.^{44,54,55}

3.5. Theoretical and Experimental XAS. The Ti K-edge X-ray absorption near edge spectroscopy (XANES) spectra (4966 eV) of nondoped and Nb-doped TiO_2 are shown in Figure 6. The absorption spectra reveal great resemblance,

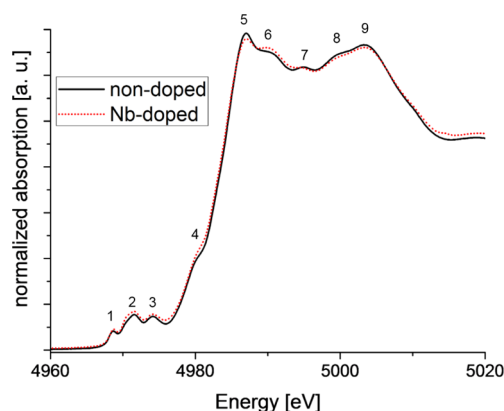


Figure 6. Measured Ti K-edge of XANES spectra of nondoped and Nb-doped TiO_2 .

having the same number of pre-edge and edge peaks as well as the same absorption edge position, merely small differences in intensity being observed. This is in good agreement with results from DFT calculations of the XAS spectra which illustrate that no significant changes of the Ti K-edge are expected under the influence of Nb doping; see Figure 7. The observed differences between the relative amplitudes of the experimental and theoretical edge features are mainly due to energy dependent broadening effects caused by the finite lifetime of the final electronic state which was not taken into account in the calculations for simplicity.

All the peaks of the experimental XANES spectra are reproduced by the calculations and can be assigned to main peaks of the Ti p DOS of the conduction band except for the

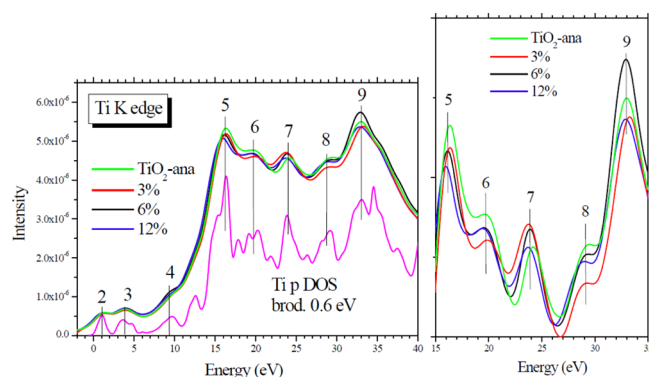


Figure 7. Theoretical XANES spectra at the K-edge of nondoped and Nb-doped anatase TiO_2 (about 3, 6, and 12 at. % of Nb). The broadened Ti p DOS is shown for comparison. The origin of energy is taken at the Fermi level.

pre-edge peak 1 which is purely quadrupolar as in the case of rutile TiO_2 .⁵⁶ The pre-edge peaks 2 and 3 contain the dipolar components and reflect the $t_{2g}-e_g$ splitting of Ti in the TiO_6 octahedral environment.

Since the comparison of XANES at the Ti K-edge of nondoped and Nb-doped anatase provides little information on the incorporation of Nb within the anatase lattice, we turned our attention to the EXAFS signal which bears information on local structure. The k^2 weighted EXAFS signal of doped and nondoped TiO_2 is shown in Figure 8a, and the derived Fourier transforms are shown in Figure 8b. The spectra of nondoped and Nb-doped TiO_2 are rather similar, indicating that local structure is largely preserved. Only a slight decrease of the amplitude of the EXAFS spectrum of the Nb-doped sample is observed, corresponding to a slight decrease of the maxima in the Fourier transform; cf. Figure 8b.

According to the crystal structure of anatase, these spectra were fitted in the R -space using one oxygen coordination shell for the closest peak and two titanium and one oxygen shell for the following ones. For the Nb-doped sample, Nb incorporation in the anatase lattice was taken into account through a combination of the FEFF Ti–Ti paths of anatase and corresponding Ti–Nb paths derived from Nb_2O_5 in which the central Nb atom was replaced by Ti. A slight variation of interatomic distances is observed upon Nb insertion (cf. Table 1), which suggests that Nb predominately occupies Ti sites. Furthermore, slightly higher Debye–Waller factors are

observed for Nb-doped than for nondoped TiO_2 , which reflects an increase in disorder of the structure due to incorporation of Nb in the anatase lattice. This explains the reduced intensity of the FT spectra of the doped sample, and confirms the substitutional doping of Nb.

The R -factor reflects the absolute misfit between experimental data and the fitted curve. Its variation as a function of the degree of Nb doping imposed during the fitting procedure follows a stretched parabolic slope with a minimum at 22 at. % Nb dopant, indicating the best agreement between measured and fitted EXAFS data; see Figure 9. This result is in line with the assumption that Nb partially substitutes Ti atoms in the anatase lattice, whereas the deviation of the peak minimum (≈ 22 at. %) from the expected Nb content (≈ 10 at. %) is considered acceptable regarding the width of the minimum and assumptions and simplifications made in the computational approach.

The partial density of states (PDOS) of Nb 4d and Ti 3d are similar, but the additional Nb 4d electron (compared to the Ti 3d electron number) pushes the Fermi level from the top of the valence band for nondoped TiO_2 to the bottom of the conduction band for Nb-doped TiO_2 , Figure 10. The lowest Nb 4d empty states are not in the band gap but overlap with Ti 3d empty states to form a band in the range 0–2 eV. The Fermi level is located within this band, which indicates that Nb-doped anatase TiO_2 has a metallic conductivity due to the delocalization of this additional Nb 4d electron as previously discussed.^{33,34,44,46,57}

Summing up the above stated findings, we can assume that the main reason for the improved rate capability of Nb-doped TiO_2 lies in the enhancement of charge transfer in TiO_2 . Substituting Ti^{4+} by aliovalent Nb^{5+} introduces additional charge carriers which improve the low bulk conductivity of TiO_2 . This effect is especially prominent at elevated cycling rates as kinetic limitations become more salient. Our results are very much in agreement with findings by Han et al.,³¹ reporting a doubling of rate capability at increased cycling rate while absolute capacities are only slightly improved for aliovalent doped TiO_2 electrospun fibers. The possibilities to compare our results to those of other groups are however limited, as few groups focus on studying the isolated effect of the dopant like we did. In most existing studies, side contributions deriving from a complex synthesis method to achieve specific morphology^{26,32,58,59} or elaborate electrode formulation^{20,60–62} are superimposing to the effect of dopant and are therefore

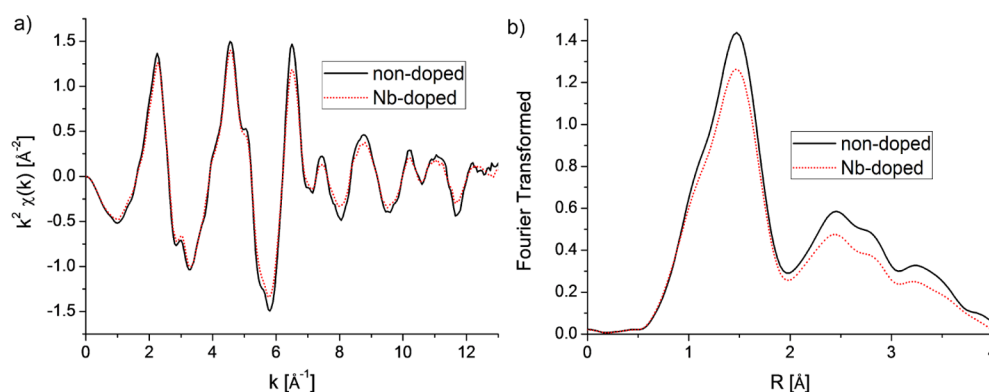
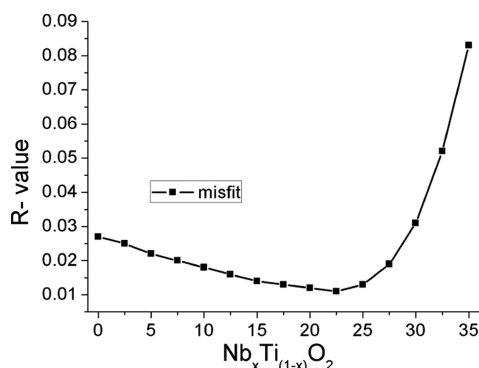
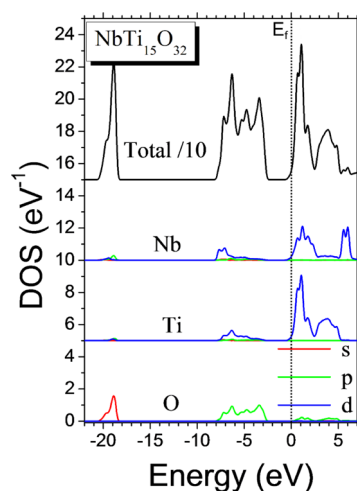


Figure 8. k^2 weighted (a) EXAFS signal and (b) Fourier transform of nondoped and doped TiO_2 nanofibers. The latter reveals the position of next neighbor shells of the central Ti atom for Nb-doped and nondoped TiO_2 .

Table 1. EXAFS Fitting Parameters for Nondoped and 10% Nb-Doped Anatase

	atom	CN	interatomic distance (Å)		Debye–Waller factor (Å ²)	
			nondoped	Nb-doped	nondoped	Nb-doped
1	O	6	1.948(±0.005)	1.949(±0.004)	0.0055(±0.0006)	0.0069(±0.0006)
2	Ti/Nb	4	3.068(±0.007)	3.068(±0.007)	0.0066(±0.0009)	0.0067(±0.0009)
3	Ti/Nb	4	3.88(±0.10)	3.85(±0.08)	0.023(±0.022)	0.020(±0.024)
4	O	8	3.844(±0.034)	3.86(±0.06)	0.004(±0.003)	0.007(±0.004)

Figure 9. Misfit of EXAFS fit as a function of the extent of Nb doping of TiO₂.Figure 10. Calculated partial densities of states of NbTi₁₅O₃₂ (≈6 at. %). The origin of energy is taken at the Fermi level (dotted line).

hardly comparable to our results. It is needless to say that a specific work on electrode formulation will probably bring rate capability and capacity retention improvements.

4. CONCLUSIONS

We showed that the Nb dopant is homogeneously distributed within the electrospun anatase fibers, and it is embedded in the lattice by substituting Ti. The statistical substitution of every 10th Ti atom by Nb has no influence on the global morphology, and only slight changes of the lattice were observed via XRD and Raman. DFT calculations and XAS experimental results go hand in hand in showing that no relevant changes of the Ti K absorption edge occur. EXAFS indicates an increased disorder in doped samples which underlines the embedding of Nb by substitutional doping in the bulk of TiO₂. Galvanostatic cycling shows that the Li insertion mechanism remains largely unaffected by niobium doping of TiO₂ anatase. However, when comparing the rate

capability, superior performance of the Nb-doped sample is evident. We ascribe this improvement predominantly to two of the observed Nb-doping induced effects: first, the global increase in the electronic conductivity which is related to the change in Fermi level position, and second, the decrease in crystal size that is beneficial for interparticle contact and reduces diffusion paths, which is crucial for high performance cycling. The ancillary effect of increasing specific surface area is likely to also contribute to the observed improvement.

AUTHOR INFORMATION

Corresponding Author

*E-mail: mfehse@um2.fr (M.F.); lorenzo.stievano@univ-montp2.fr (L.S.). Phone: +33 467 143 346 (L.S.).

Notes

The authors declare no competing financial interest.

ACKNOWLEDGMENTS

The authors are grateful for financial support by Saft and CNRS. Access to synchrotron radiation facilities of ELETTRA (XAFS beamline) and Desy (Beamline A) is acknowledged. The authors would like to thank Luca Olivi, Giuliana Aquilanti, and Edmund Welter for expert advice on beamline operation. Furthermore, the research leading to these results has received funding from the European Research Council under the European Union's Seventh Framework Programme (FP/2007-2013)/ERC Grant Agreement No. 306682.

REFERENCES

- (1) Yoshino, A. The Birth of the Lithium-Ion Battery. *Angew. Chem.* **2012**, *51*, 5798–5800.
- (2) Deng, D.; Kim, M. G.; Lee, J. Y.; Cho, J. Green Energy Storage Materials: Nanostructured TiO₂ and Sn-Based Anodes for Lithium-Ion Batteries. *Energy Environ. Sci.* **2009**, *2*, 818–837.
- (3) Kerisit, S.; Rosso, K. M.; Yang, Z.; Liu, J. Dynamics of Coupled Lithium/Electron Diffusion in TiO₂ Polymorphs. *J. Phys. Chem. C* **2009**, *113*, 20998–21007.
- (4) Kyeremateng, N.; Vacandio, F.; Sougrati, M.-T.; Martinez, H.; Jumas, J.-C.; Knauth, P.; Djenizian, T. Effect of Sn-Doping on the Electrochemical Behaviour of TiO₂ Nanotubes as Potential Negative Electrode Materials for 3D Li-Ion Micro Batteries. *J. Power Sources* **2013**, *224*, 269–277.
- (5) Nowotny, J. In *Oxide Semiconductors for Solar Energy Conversion*; TiO₂; Lee, S., Ed.; CRC Press: Boca Raton, FL, 2012; p 414.
- (6) Shin, J.-y.; Joo, J. H.; Samuelis, D.; Maier, J. Oxygen-Deficient TiO₂ Nanoparticles via Hydrogen Reduction for High Rate Capability Lithium Batteries. *Chem. Mater.* **2012**, *24*, 543–551.
- (7) Xia, Y.; Yang, P.; Sun, Y.; Wu, Y.; Mayers, B.; Gates, B.; Yin, Y.; Kim, F.; Yan, H. One-Dimensional Nanostructures: Synthesis, Characterization, and Applications. *Adv. Mater.* **2003**, *15*, 353–389.
- (8) Barth, S.; Hernandez-Ramirez, F.; Holmes, J. D.; Romano-Rodriguez, A. Synthesis and Applications of One-Dimensional Semiconductors. *Prog. Mater. Sci.* **2010**, *55*, 563–627.
- (9) Cheng, F.; Tao, Z.; Liang, J.; Chen, J. Template-Directed Materials for Rechargeable Lithium-Ion Batteries. *Chem. Mater.* **2008**, *20*, 667–681.

- (10) Tarascon, J.-M.; Reham, N.; Armand, M.; Chotard, J.-N.; Barpanda, P.; Walker, W.; Dupont, L. Hunting for Better Li-Based Electrode Materials via Low Temperature Inorganic Synthesis. *Chem. Mater.* **2010**, *22*, 724–739.
- (11) Kasuga, T.; Hiramatsu, M.; Hoson, A.; Sekino, T. Formation of Titanium Oxide Nanotube. *Langmuir* **1998**, *14*, 3160–3163.
- (12) Zhao, B.; Shao, Z. From Paper to Paper-Like Hierarchical Anatase TiO₂ Film Electrode for High-Performance Lithium-Ion Batteries. *J. Phys. Chem. C* **2012**, *116*, 17440–17447.
- (13) Reneker, D.; Yarin, A.; Zussman, E.; Xu, H. Electrospinning of Nanofibers from Polymer Solutions and Melts. *Adv. Appl. Mech.* **2007**, *41*, 44–197.
- (14) Sawicka, K. M.; Gouma, P. Electrospun Composite Nanofibers for Functional Applications. *J. Nanopart. Res.* **2006**, *8*, 769–781.
- (15) Dai, Y.; Liu, W.; Formo, E.; Sun, Y.; Xia, Y. Ceramic Nanofibers Fabricated by Electrospinning and Their Applications in Catalysis, Environmental Science, and Energy Technology. *Polym. Adv. Technol.* **2011**, *22*, 326–338.
- (16) Cavaliere, S.; Subianto, S.; Savych, I.; Jones, D. J.; Rozière, J. Electrospinning: Designed Architectures for Energy Conversion and Storage Devices. *Energy Environ. Sci.* **2011**, *4*, 4761–4785.
- (17) Cavaliere, S.; Subianto, S.; Chevallier, L.; Jones, D. J.; Rozière, J. Single Step Elaboration of Size-Tuned Pt Loaded Titania Nanofibers. *Chem. Commun.* **2011**, *47*, 6834–6836.
- (18) Bauer, A.; Chevallier, L.; Hui, R.; Cavaliere, S.; Zhang, J.; Jones, D.; Rozière, J. Synthesis and Characterization of Nb-TiO₂ Mesoporous Microsphere and Nanofiber Supported Pt Catalysts for High Temperature PEM Fuel Cells. *Electrochim. Acta* **2012**, *77*, 1–7.
- (19) Luo, W.; Hu, X.; Sun, Y.; Huang, Y. Surface Modification of Electrospun TiO₂ Nanofibers via Layer-by-Layer Self-Assembly for Highperformance Lithium-Ion Batteries. *J. Mater. Chem.* **2012**, *22*, 4910–4915.
- (20) Zhu, P.; Wu, Y.; Reddy, M. V.; Sreekumaran Nair, A.; Chowdari, B. V. R.; Ramakrishna, S. Long Term Cycling Studies of Electrospun TiO₂ Nanostructures and Their Composites with MWCNTs for Rechargeable Li-Ion Batteries. *RSC Adv.* **2012**, *2*, 531–537.
- (21) Yang, X.; Teng, D.; Liu, B.; Yu, Y.; Yang, X. Nanosized Anatase Titanium Dioxide Loaded Porous Carbon Nanofiber Webs as Anode Materials for Lithium-Ion Batteries. *Electrochem. Commun.* **2011**, *13*, 1098–1101.
- (22) Feng, C.; Tang, J.; Zhang, C.; Zeng, R. Synthesis and Electrochemical Properties of TiO₂/C Nano-Fiber Composite. *Nanosci. Nanotechnol. Lett.* **2012**, *4*, 430–434.
- (23) Zhang, X.; Kumar, P. S. Electrospun TiO₂-Graphene Composite Nanofibers as Highly Durable Insertion Anode for Lithium-Ion Batteries. *J. Phys. Chem. C* **2012**, *116*, 14780–14788.
- (24) Manthiram, A.; Vadivel Murugan, A.; Sarkar, A.; Muraliganth, T. Nanostructured Electrode Materials for Electrochemical Energy Storage and Conversion. *Energy Environ. Sci.* **2008**, *1*, 621–638.
- (25) Nam, S. H.; Shim, H.-S.; Kim, Y.-S.; Dar, M. A.; Kim, J. G.; Kim, W. B. Ag or Au Nanoparticle-Embedded One-Dimensional Composite TiO₂ Nanofibers Prepared via Electrospinning for Use in Lithium-Ion Batteries. *ACS Appl. Mater. Interfaces* **2010**, *2*, 2046–2052.
- (26) Yuan, T.; Zhao, B.; Cai, R.; Zhou, Y.; Shao, Z. Electrospinning Based Fabrication and Performance Improvement of Film Electrodes for Lithium-Ion Batteries Composed of TiO₂ Hollow Fibers. *J. Mater. Chem.* **2011**, *21*, 15041–15048.
- (27) Jin, M.; Zhang, X.; Pu, H.; Nishimoto, S.; Murakami, T.; Fujishima, A. Photochromism-Based Detection of Volatile Organic Compounds by W-Doped TiO₂ Nanofibers. *J. Colloid Interface Sci.* **2011**, *362*, 188–93.
- (28) Babu, V. J.; Nair, A. S.; Peining, Z.; Ramakrishna, S. Synthesis and Characterization of Rice Grains Like, Nitrogen-Doped TiO₂ Nanostructures by Electrospinning-Photocatalysis. *Mater. Lett.* **2011**, *65*, 3064–3068.
- (29) Park, J.-Y.; Lee, J.-H.; Choi, D.-Y.; Hwang, C.-H.; Lee, J.-W. Influence of Fe Doping on Phase Transformation and Crystallite Growth of Electrospun TiO₂ Nanofibers for Photocatalytic Reaction. *Mater. Lett.* **2012**, *88*, 156–159.
- (30) Bingham, S.; Daoud, W. a. Recent Advances in Making Nanosized TiO₂ Visible-Light Active through Rare-Earth Metal Doping. *J. Mater. Chem.* **2011**, *21*, 2041–2050.
- (31) Han, H.; Song, T.; Bae, J.-Y.; Nazar, L. F.; Kim, H.; Paik, U. Nitridated TiO₂ Hollow Nanofibers as an Anode Material for High Power Lithium Ion Batteries. *Energy Environ. Sci.* **2011**, *4*, 4532–4536.
- (32) Wang, Y.; Smarsly, B. M.; Djerdj, I. Niobium Doped TiO₂ with Mesoporosity and Its Application for Lithium Insertion. *Chem. Mater.* **2010**, *22*, 6624–6631.
- (33) Archana, P. S.; Jose, R.; Jin, T. M.; Vijila, C.; Yusoff, M. M.; Ramakrishna, S. Structural and Electrical Properties of Nb-Doped Anatase TiO₂ Nanowires by Electrospinning. *J. Am. Ceram. Soc.* **2010**, *93*, 4096–4102.
- (34) Sheppard, L. R.; Bak, T.; Nowotny, J. Electrical Properties of Niobium-Doped Titanium Dioxide. 1. Defect Disorder. *J. Phys. Chem. B* **2006**, *110*, 22447–22454.
- (35) Perdew, J.; Burke, K.; Ernzerhof, M. Generalized Gradient Approximation Made Simple. *Phys. Rev. Lett.* **1996**, *77*, 3865–3868.
- (36) Blaha, P.; Schwarz, K.; Madsen, G.; Kvasnicka, D.; Luitz, J. WIEN2K An Augmented Plane Wave Plus Local Orbitals Program for Calculating Crystal Properties; Technische Universität Wien: Wien, Austria, 2001.
- (37) Weibel, A.; Bouchet, R.; Savin, S. L. P.; Chadwick, A. V.; Lippens, P. E.; Womes, M.; Knauth, P. Local Atomic and Electronic Structure in Nanocrystalline Sn-Doped Anatase TiO₂. *ChemPhysChem* **2006**, *7*, 2377–2383.
- (38) Lippens, P.; Chadwick, A. Structure and Chemical Bonding in Zr-Doped Anatase TiO₂ Nanocrystals. *J. Phys. Chem. C* **2008**, *112*, 43–47.
- (39) Lippens, P.-E.; Womes, M.; Kubiak, P.; Jumas, J.-C.; Olivier-Fourcade, J. Electronic Structure of the Spinel Li₄Ti₅O₁₂ Studied by Ab Initio Calculations and X-ray Absorption Spectroscopy. *Solid State Sci.* **2004**, *6*, 161–166.
- (40) An, H.; Ahn, H.-J. Fabrication of Wrinkled Nb-Doped TiO₂ Nanofibers via Electrospinning. *Mater. Lett.* **2013**, *93*, 88–91.
- (41) Sing, K. S. W. Reporting Physisorption Data for Gas/Solid Systems with Special Reference to the Determination of Surface Area and Porosity. *Pure Appl. Chem.* **1982**, *54*, 2201–2218.
- (42) Ruiz, A. M.; Dezanneau, G.; Arbiol, J.; Cornet, A.; Morante, J. R. Insights into the Structural and Chemical Modifications of Nb Additive on TiO₂ Nanoparticles. *Chem. Mater.* **2004**, *16*, 862–871.
- (43) Guidi, V.; Carotta, M. Effect of Dopants on Grain Coalescence and Oxygen Mobility in Nanostructured Titania Anatase and Rutile. *J. Phys. Chem. B* **2003**, *107*, 120–124.
- (44) Furubayashi, Y.; Hitosugi, T.; Yamamoto, Y.; Inaba, K.; Kinoda, G.; Hirose, Y.; Shimada, T.; Hasegawa, T. A Transparent Metal: Nb-Doped Anatase TiO₂. *Appl. Phys. Lett.* **2005**, *86*, 252101–252103.
- (45) Hirano, M.; Ichihashi, Y. Phase Transformation and Precipitation Behavior of Niobium Component out of Niobium-Doped Anatase-Type TiO₂ Nanoparticles Synthesized via Hydrothermal Crystallization. *J. Mater. Sci.* **2009**, *44*, 6135–6143.
- (46) Yang, Z.; Choia, D.; Kerisit, S.; Rosso, K. M.; Wang, D.; Zhang, J.; Graff, G.; Liu, J. Nanostructures and Lithium Electrochemical Reactivity of Lithium Titanates and Titanium Oxides: A Review. *J. Power Sources* **2009**, *192*, 588–598.
- (47) Baddour-Hadjean, R.; Pereira-Ramos, J.-P. Raman Microspectrometry Applied to the Study of Electrode Materials for Lithium Batteries. *Chem. Rev.* **2010**, *110*, 1278–1319.
- (48) Lejon, C.; Österlund, L. Influence of Phonon Confinement, Surface Stress, and Zirconium Doping on the Raman Vibrational Properties of Anatase TiO₂ Nanoparticles. *J. Raman Spectrosc.* **2011**, *42*, 2026–2035.
- (49) Kuznetsov, M. V.; Zhuravlev, J. F.; Zhilyaev, V. A.; Gubanov, V. A. XPS Study of the Nitrides, Oxides and Oxynitrides of Titanium. *J. Electron Spectrosc. Relat. Phenom.* **1992**, *58*, 1–9.
- (50) Bahl, M. ESCA Studies of Some Niobium Compounds. *J. Phys. Chem. Solids* **1975**, *36*, 485–491.

(51) Wang, P.; Wu, J.; Ao, Y.; Wang, C.; Hou, J.; Qian, J. Preparation and Enhanced Photocatalytic Performance of Sn Ion Modified Titania Hollow Spheres. *Mater. Lett.* **2011**, *65*, 3278–3280.

(52) Sheppard, L. R.; Dittrich, T.; Nowotny, M. K. The Impact of Niobium Surface Segregation on Charge Separation in Niobium-Doped Titanium Dioxide. *J. Phys. Chem. C* **2012**, *116*, 20923–20929.

(53) Ehinon, K. K. D.; Naille, S.; Dedryve, R.; Lippens, P. E.; Jumas, J.-C.; Gonbeau, D. Ni₃Sn₄ Electrodes for Li-Ion Batteries: Li-Sn Alloying Process and Electrode/Electrolyte Interface Phenomena. *Chem. Mater.* **2008**, *20*, 5388–5398.

(54) Knauth, P.; Chadwick, A. V.; Lippens, P. E.; Auer, G. EXAFS Study of Dopant Ions with Different Charges in Nanocrystalline Anatase: Evidence for Space-Charge Segregation of Acceptor Ions. *ChemPhysChem* **2009**, *10*, 1238–46.

(55) Bouchet, R.; Weibel, A.; Knauth, P. EXAFS Study of Dopant Segregation (Zn, Nb) in Nanocrystalline Anatase (TiO₂). *Chem. Mater.* **2003**, *15*, 4996–5002.

(56) Joly, Y.; Cabaret, D.; Renevier, H.; Natoli, C. Electron Population Analysis by Full-Potential X-Ray Absorption Simulations. *Phys. Rev. Lett.* **1999**, *82*, 2398–2401.

(57) Hitosugi, T.; Kamisaka, H.; Yamashita, K.; Nogawa, H.; Furubayashi, Y.; Nakao, S.; Yamada, N.; Chikamatsu, A.; Kumigashira, H.; Oshima, M.; Hirose, Y.; Shimada, T.; Hasegawa, T. Electronic Band Structure of Transparent Conductor: Nb-Doped Anatase TiO₂. *Appl. Phys. Express* **2008**, *1*, 111203–06.

(58) Ali, Z.; Cha, S. N.; Sohn, J. I.; Shakir, I.; Yan, C.; Kim, J. M.; Kang, D. J. Design and Evaluation of Novel Zn Doped Mesoporous TiO₂ Based Anode Material for Advanced Lithium Ion Batteries. *J. Mater. Chem.* **2012**, *22*, 17625.

(59) Das, S. K.; Gnanavel, M.; Patel, M. U. M.; Shivakumara, C.; Bhattacharyya, A. J. Anomolously High Lithium Storage in Mesoporous Nanoparticulate Aggregation of Fe³⁺ Doped Anatase Titania. *J. Electrochem. Soc.* **2011**, *158*, A1290.

(60) Ding, Y.-H.; Zhang, P.; Ren, H.-M.; Zhuo, Q.; Yang, Z.-M.; Jiang, Y. Preparation of Graphene/TiO₂ Anode Materials for Lithium-Ion Batteries by a Novel Precipitation Method. *Mater. Res. Bull.* **2011**, *46*, 2403–2407.

(61) Yang, Z.; Du, G.; Meng, Q.; Guo, Z.; Yu, X.; Chen, Z.; Guo, T.; Zeng, R. Synthesis of Uniform TiO₂@Carbon Composite Nanofibers as Anode for Lithium Ion Batteries with Enhanced Electrochemical Performance. *J. Mater. Chem.* **2012**, *22*, 5848.

(62) Cao, F.-F.; Xin, S.; Guo, Y.-G.; Wan, L.-J. Wet Chemical Synthesis of Cu/TiO₂ Nanocomposites with Integrated Nano-Current-Collectors As High-Rate Anode Materials in Lithium-Ion Batteries. *Phys. Chem. Chem. Phys.* **2011**, *13*, 2014–20.